Effect of Orifice Geometry and Air-Inlet Position on Air–Water Entrainment: A CFD Study

Mohammed H. Salih[1*], Mostafa Ali Abdelaal [1], Rani Fouad Mohammed [2], Adel A. Elshimy[2], Ahmed H. Mahmoud[3]

[1]Department of Civil Engineering, Faculty of Engineering, University of Anbar, Ramadi 31001, Iraq
[2] Department of Civil Engineering, Faculty of Engineering, Al-Azhar University, Cairo 4450113, Egypt
[3] Department of Civil Engineering, Faculty of Engineering, Al-Azhar University, Cairo 4450113, Egypt

Abstract
Orifice-induced air entrainment plays an important role in hydraulic aeration, mixing systems, and energy dissipation devices. However, the combined influence of orifice geometry and air-inlet location on air–water entrainment characteristics remains insufficiently understood. Therefore, this study presents a combined experimental and computational investigation of air–water discharge through circular, square, and triangular sharp-edged orifices with different opening dimensions and air-inlet configurations. Approximately 120 numerical and experimental cases are examined under a wide range of Reynolds numbers. A three-dimensional CFD model is developed in ANSYS Fluent using the Volume of Fluid (VOF) multiphase approach coupled with the realizable k–ε turbulence model. The numerical predictions are validated against experimental measurements, showing good agreement with most deviations remaining within a few percent. The results show that reducing the orifice opening enhances the normalized discharge ratio $R = \left(\frac{Q_a}{Q_w}\right)$ by increasing jet acceleration, pressure reduction, and suction near the vena contracta. Considering the circular orifice as baseline design, triangular orifices achieved the highest entrainment performance, with normalized ratios $R^* = 1.239–2.189$, corresponding to improvements of 23.9–118.9% over the baseline circular case. Square orifices showed moderate enhancement, with $R^* = 0.814–1.322$ and a maximum improvement of 32.2%. Forward shifting the air inlet in circular orifices produced $R^* = 0.520–1.099$, indicating that inlet relocation can improve entrainment by up to 9.9%.

Keywords: Air–water entrainment; CFD simulation; Circular orifice; Discharge ratio; Orifice plate; Square orifice; Triangular orifice

1 Introduction

Orifice plates are widely used in hydraulic engineering for flow control, discharge measurement, energy dissipation, and aeration enhancement owing to their simple geometry and adaptability to conduits, aeration systems, and water and wastewater treatment facilities. Accordingly, numerous studies have employed computational fluid dynamics (CFD) [1], [2], [3] to investigate orifice-based systems [4], [5], [6]. Jothiprakash et al. [4] developed and experimentally validated a three-dimensional two-phase model for flow over orifice spillway aerators, showing that aerator offset distance and chute slope strongly affect air entrainment and energy dissipation. Similarly, Sarwar et al. [7] combined experiments and three-dimensional CFD simulations for the Bunji Dam orifice aerator and related lip height, cavity length, and orifice configuration to dimensionless air demand and pressure distribution. CFD has also been applied to full-scale aeration and jet-flow systems. Höhne and Mamedov [8] used a three-dimensional Eulerian–multiphase model with the SST turbulence model in ANSYS CFX to examine aeration and mixing in a full-scale oxidation ditch. Cao et al. [9] applied steady RANS simulations with the realizable k–ε model in ANSYS Fluent to analyze jet discharge from slot orifices in perforated air ducts.

Further studies have assessed CFD accuracy and limitations in orifice-flow prediction. Tukiman et al. [10] validated CFD predictions of pressure drop and discharge coefficient against experiments and showed that reliable results require careful control of mesh resolution and turbulence modeling. Fadaei et al. [11] extended CFD–experimental analysis to gas–liquid two-phase orifice flow, reporting increasing deviations from single-phase correlations with higher gas void fractions. Hernandez-Perez et al. [12] highlighted grid-generation and interface-capturing issues in two-phase pipe-flow CFD, showing that inadequate refinement near the vena contracta and gas–liquid interface can cause numerical artifacts and pressure-drop errors. Golijanek-Jędrzejczyk et al. [13] combined experiments with SolidWorks Flow Simulation to study segmental orifices at Reynolds numbers of 9,000–17,000. Their model captured recirculation zones, pressure-drop distributions, and downstream flow structures, with numerical deviations below 5.1% and measurement uncertainties below 1.8%. Medeiros et al. [14] showed that discharge coefficients and volumetric-flow estimates are highly sensitive to plate dimensions, edge sharpness, and pipe-wall roughness.

Experimental studies have also clarified key geometric effects. Jitschin [15] showed that thin circular orifices produce substantial permanent pressure losses, whereas Venturi tubes provide lower losses and more stable flow-measurement performance, emphasizing the importance of edge geometry and upstream flow conditioning. More recently, Eltoukhy and Alsaydalani [16] found that the discharge coefficient decreases with increasing orifice length and increases with larger diameters, indicating limitations in constant-coefficient correlations and the need for geometry- and regime-dependent predictive models.

Dhumal et al. [17] used ANSYS CFD to compare single-hole and multi-hole orifice plates with 4, 5, and 7 holes. They showed that multi-hole configurations reduce turbulence intensity and improve downstream flow uniformity, with the 5-hole plate providing the closest agreement with discharge measurements and lower pressure losses than the conventional single-hole plate. Almutairi et al. [18] further demonstrated that hole arrangement, porosity, and pitch ratio strongly affect discharge coefficients, flow stability, and pressure recovery in multi-hole orifice meters. Related CFD studies by Singh and Tharakan [19] and Düz [20] examined perforated multi-hole plates and optimized bevel angles for conical-entrance multi-hole orifices, respectively. Venturi tubes and venturi-type aerators provide a useful basis for understanding contraction-induced pressure reduction and air entrainment. Baylar [21] showed that venturi weirs can operate as efficient aerators, with throat geometry and upstream head controlling air intake and oxygen transfer. Yadav et al. [22] demonstrated that converging and diverging angles, throat length, and velocity distribution strongly influence suction capacity and flow stability. Subsequent studies confirmed the robustness and energy efficiency of venturi aeration systems by quantifying oxygen transfer rate, standard oxygen transfer rate, and aeration efficiency under different operating conditions [23].

Aeration in hydraulic structures offers a close analogy to orifice-induced aeration in discharged flows. Aydin and Ulu [24] used CFD to resolve two-phase flow in siphon-shaft spillways, showing that aerator geometry affects air concentration and cavitation indices. Their simulations also captured the vena contracta and agreed well with experimental observations. Guo et al. [25] showed that ambient pressure substantially affects aeration behavior, particularly under high-altitude conditions. Studies on stepped spillways, cascades, and aerating chutes further demonstrated that step geometry and slope govern air entrainment, void fraction, oxygen transfer, and mass-transfer coefficients [26], [27]. Jet-aeration studies have also highlighted the role of outlet geometry. Bagatur et al. [28] showed that nozzle shape strongly affects bubble entrainment and penetration depth by altering shear-layer characteristics, which is directly relevant to shaped orifice plates. Baawain and Radkevich [29] identified optimal jet velocities and diameters for maximizing aeration efficiency, whereas Puri et al. [30] combined experimental data and artificial-intelligence methods to predict aeration efficiency over broad parameter ranges.

Despite extensive research on orifice plates, previous studies have mainly addressed circular geometries, multi-hole configurations, or isolated design parameters. Limited attention has been given to the comparative hydraulic performance of different single-hole orifice shapes under consistent operating conditions. Moreover, the combined effects of orifice geometry, diameter, and geometric proportions on flow structure, pressure distribution, discharge characteristics, and air–water interaction remain insufficiently understood, particularly for aeration and energy-dissipation applications. Therefore, this study develops and experimentally validates a CFD model to systematically investigate flow through orifice plates with different shapes and diameters. The validated model is then applied to parametric cases to evaluate the effects of orifice geometry and proportions on velocity fields and discharge coefficients. The novelty of this work lies in establishing a unified comparative CFD framework for assessing multiple orifice geometries using consistent numerical and experimental methods, thereby supporting improved design and optimization of hydraulic and aeration systems.

2 Building of Numerical model

Numerical simulations are performed in ANSYS Fluent to investigate transient multiphase flow through the examined orifice geometries. Because the flow involves the interaction of immiscible water and air separated by a distinct interface, it is modeled as a two-phase system using the VOF approach. This model is selected for its ability to capture sharp gas–liquid interfaces and account for the large density and viscosity differences between the phases, which are critical for predicting jet development, pressure distribution, recirculation, and air entrainment downstream of the orifice.

The governing equations are solved under transient conditions using a fixed time-step scheme with 2000 maximum time steps, a time-step size of 0.1 s, and a maximum of 20 iterations per time step. This time-step size is selected to maintain numerical stability and accuracy relative to the experimental results while minimizing computational cost. Turbulence is modeled using the realizable k–ε model with scalable wall functions because of its robustness in predicting turbulent jets, flow separation, recirculation zones, and shear-layer development downstream of sharp-edged orifices [31]. The gravity acceleration is defined in the vertical direction with a value of $9.81\,\frac{\mathrm{m}}{\mathrm{s}^2}$.

2.1 Governing Equations

The VOF model solves a single set of momentum equations for the mixture while tracking the water–air interface through the transport of phase volume fractions. The governing equations include the continuity, momentum conservation, turbulence transport, and secondary-phase volume-fraction equations. [32].

The continuity equation for incompressible flow is expressed as:

$$\nabla \cdot \mathbf{u} = 0 \tag{1}$$

where $\mathbf{u}$ is the velocity vector.

The transient momentum conservation equation for the multiphase mixture is given by:

$$\frac{\partial(\rho \mathbf{u})}{\partial t} + \nabla \cdot (\rho \mathbf{u}\mathbf{u}) = -\nabla p + \nabla \cdot [\mu(\nabla \mathbf{u} + (\nabla \mathbf{u})^{T})] + \rho \mathbf{g} + \mathbf{F} \tag{2}$$

where p denotes the pressure, ρ is the mixture density, μ defines the dynamic viscosity, $\mathbf{g}$ is the gravitational acceleration vector, and $\mathbf{F}$ represents body-force terms including surface tension effects if considered.

Within the VOF formulation, the volume fraction equation for the water phase is solved as:

$$\frac{\partial \alpha_w}{\partial t} + \nabla \cdot (\alpha_w \mathbf{u}) = 0 \quad (3)$$

where α_w is the water volume fraction. The air volume fraction is determined from:

$$\alpha_a = 1 - \alpha_w \quad (4)$$

The mixture density and viscosity are evaluated according to the phase volume fractions such as:

$$\rho = \alpha_w \rho_w + \alpha_a \rho_a \quad (5)$$

$$\mu = \alpha_w \mu_w + \alpha_a \mu_a \quad (6)$$

where subscripts w and a denote water and air phases, respectively.

Turbulence effects are modeled using the realizable $k - \varepsilon$ turbulence model. The turbulent kinetic energy k equation is expressed as:

$$\frac{\partial (\rho k)}{\partial t} + \nabla \cdot (\rho k \boldsymbol{u}) = \nabla \cdot \left[\left(\mu + \frac{\mu_t}{\sigma_k} \right) \nabla k \right] + G_k + G_b - \rho \varepsilon - Y_M \quad (7)$$

The turbulence dissipation rate ε equation is given by:

$$\frac{\partial (\rho \varepsilon)}{\partial t} + \nabla \cdot (\rho \varepsilon \boldsymbol{u}) = \nabla \cdot \left[\left(\mu + \frac{\mu_t}{\sigma_\varepsilon} \right) \nabla \varepsilon \right] + \rho C_1 S \varepsilon - \rho C_2 \frac{\varepsilon^2}{k + \sqrt{\nu \varepsilon}} \quad (8)$$

where G_k represents turbulence production due to velocity gradients, G_b is turbulence generation due to buoyancy, μ_t is the turbulent viscosity, and C_1, C_2, σ_k, and σ_ε are empirical model constants.

The realizable $k - \varepsilon$ model is selected because of its improved capability in predicting jet flows, separated flow regions, recirculation zones, and turbulent shear-layer development downstream of sharp-edged orifices. Combined with the VOF multiphase formulation and refined mesh discretization near the vena contracta and gas–liquid interface.

2.2 Computational Domain and Boundary Conditions

A series of CFD simulations is performed to investigate flow characteristics through orifices with different geometries and sizes. Three orifice shapes—circular, square, and equilateral triangular—are analyzed to assess the effect of geometry on flow behavior. For each shape, three equivalent orifice areas are considered to enable consistent comparison across cross-sections and isolate shape effects from size effects. The selected dimensions and corresponding areas used in the simulations are presented in Table 1.

Table 1. Orifices Parameters Orifice parameters for triangular and square

Orifice Shape	Orifice Dimensions	Orifice Area
Circular	Diameter = 7.5 mm.	Orifice Area = 44.16 mm^2.
Square	Side Length = 6.7 mm.	
Equilateral Triangular	Side Length = 10 mm.	
Circular	Diameter = 10 mm.	Orifice Area = 78.5 mm^2.
Square	Side Length = 8.9 mm.	
Equilateral Triangular	Side Length = 13.4 mm.	
Circular	Diameter = 12.5 mm.	Orifice Area = 122.66 mm^2.
Square	Side Length = 11.1 mm.	
Equilateral Triangular	Side Length = 16.8 mm.	

A comprehensive parametric study is conducted to examine the hydraulic behavior of circular, square, and triangular sharp-edged orifice plates under different flow conditions. For each geometry, three equivalent opening areas of 44.16, 78.50, and 122.66 mm² are considered to enable consistent shape-based comparison. The corresponding dimensions are 7.5, 10.0, and 12.5 mm for circular-orifice diameters; 6.7, 8.9, and 11.1 mm for square-orifice side lengths; and 10.0, 13.4, and 16.8 mm for triangular-orifice side lengths. CFD simulations and experimental measurements are performed at multiple flow rates to evaluate the effects of orifice shape and size on velocity distribution, discharge coefficient, and air–water interaction. Additional parametric simulations are conducted for the circular orifice by varying the air-pipe position relative to the orifice to assess its influence on air entrainment, mixing, and downstream hydraulic performance.

The computational domain consisted of a horizontal main pipe with an internal diameter of 25 mm and an orifice plate located near the junction with a vertical air-injection tube. The upstream pipe length is 90 mm, whereas the downstream section extended 150 mm from the orifice. An 8 mm diameter, 100 mm long vertical air-inlet pipe is connected perpendicular to the main pipe at 10 mm from the orifice plate to enable gas–liquid interaction in the mixing region. Water entered the main pipe through a velocity-inlet boundary derived from the prescribed mass flow rate. The air inlet is modeled as a pressure inlet to represent passive air induction, and the downstream boundary is defined as a pressure outlet to allow the two-phase mixture to exit the domain. As shown in Figure 1,

this configuration enables interface formation and captures multiphase mixing driven by the orifice-induced pressure drop and air entrainment.

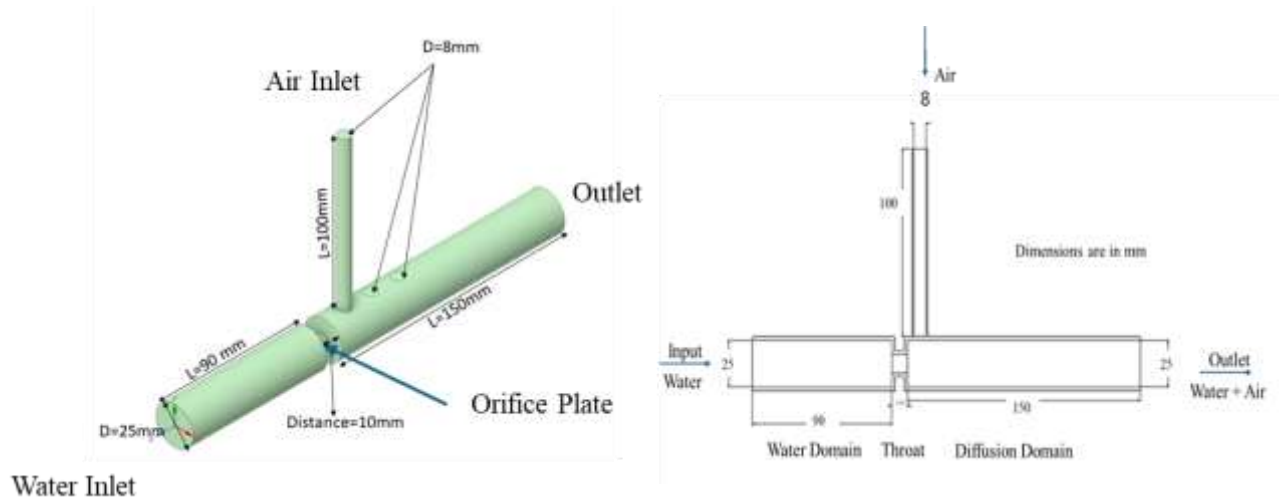

Figure 1. Model Geometry and BCs.

The working-fluid properties are defined under standard conditions. Air is modeled with a constant density of 1.225 kg/m³ and dynamic viscosity of 1.7894 × 10^{-5} kg/(m·s), whereas liquid water is assigned a density of 998.2 kg/m³ and dynamic viscosity of 0.001003 kg/(m·s).

A fine computational mesh is generated with local refinement near the orifice, vena contracta, and gas–liquid interaction regions to resolve steep pressure and velocity gradients and turbulent mixing structures. This refinement enabled accurate prediction of jet contraction, downstream recirculation, pressure drop, and air–water interaction while maintaining convergence and transient solution stability. The final mesh, shown in Figure 3, consisted of 743,663 elements and 140,197 nodes and is selected through a mesh-independence study in which the mesh density is progressively increased until the numerical results showed good agreement with the experimental data. The mesh-independence results are presented in Figure 2 and

Table ***2***.

Table 2. Mesh independent Study.

Mesh	**Elements**	Q_{air_Exp} $[x10^{-4}]$	**R**
01	495,836	2.531	0.516
02	563,235	2.367	0.482
03	642,571	1.959	0.399
04	743,663	2.1	0.428
05	789,770	2.1	0.428

$*R = \frac{Q_{air}}{Q_{water}}$

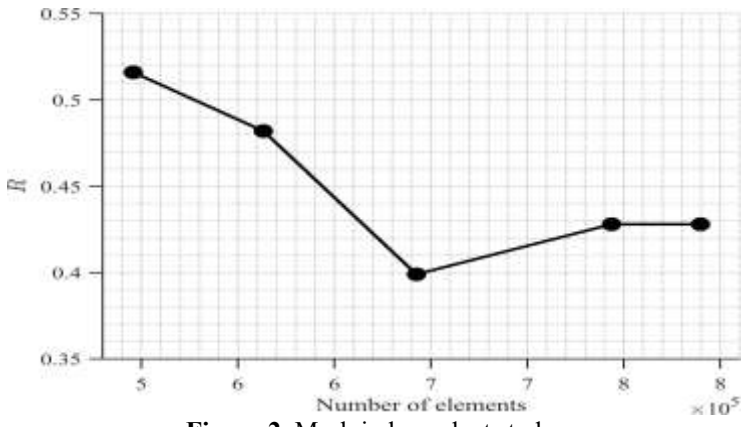

Figure 2. Mesh independent study.

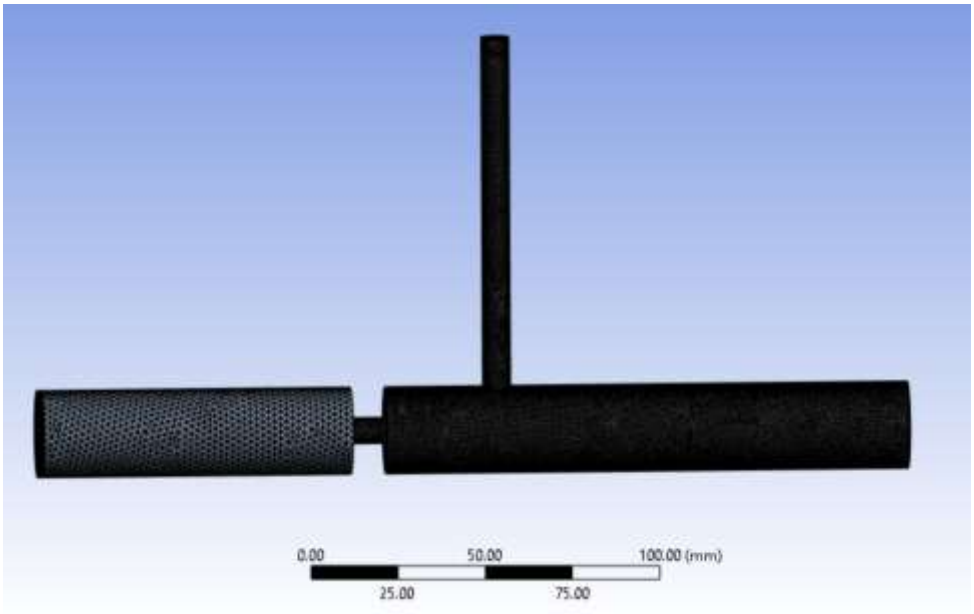

Figure 3. Domain mesh.

3 Model Validation

To validate the CFD simulations, an equivalent experimental model is developed and the numerical and experimental results are compared. The setup consisted of a closed-loop water-circulation system designed to examine two-phase flow through the orifice configuration and provide validation data for the numerical model. Water is supplied from a storage tank and pumped through a horizontal PVC pipeline supported by a rigid steel frame, as shown in Figure 4. Upstream of the test section, an inline flowmeter measured the flow rate, while a pressure gauge and digital pressure transducer recorded the pressure variation across the orifice region. The test section included a transparent segment for visual observation of the flow regime and air entrainment downstream of the orifice plate. A vertical air-injection line introduced air into the main pipeline to form gas–liquid mixtures. During each test, the water flow rate and inlet air pressure are adjusted to match the numerical boundary conditions, and steady-state measurements of pressure drop, flow rate, and flow pattern are recorded. The experimental data are then compared with the CFD predictions to validate the multiphase model based on discharge-ratio agreement.

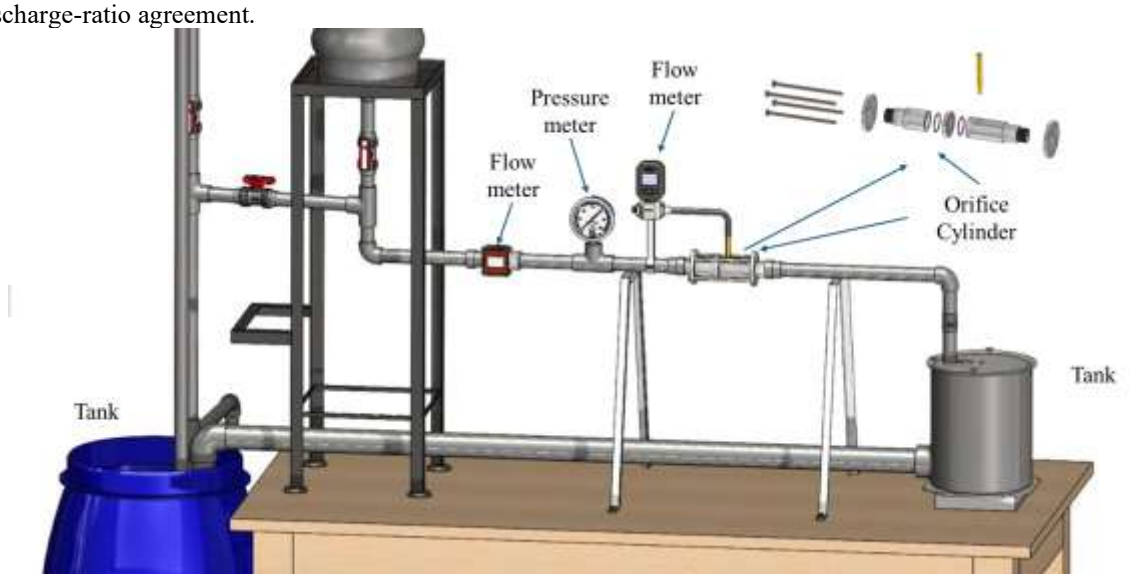

Figure 4. Experimental setup.

The effects of changing the orifice diameter and water inlet flow rate on the flow behavior are examined. Five inlet flow rates are considered, namely Q_1 = 29.44 L/min, Q_2 = 44.16 L/min, Q_3 = 58.88 L/min, Q_4 = 73.59 L/min, and Q_5 = 88.31 L/min. In addition, three different orifice geometries including circular, triangular, and square are investigated. This parametric study allows for a systematic comparison of the influence of flow rate and orifice shape on the resulting flow characteristics. The results will be presented in the form of graphs illustrating the relationship between the Reynolds number and the ratio of air to water flow rates. The Reynolds number is calculated for each inlet velocity to characterize the flow regime and assess its influence on the discharge performance of the orifice. It is determined using the standard equation:

$$Re = \frac{\rho V d}{\mu} \quad (9)$$

Where

ρ is water density = 1000 kg/m³
V water inlet velocity
d diameter of the pipe = 25 mm and
μ dynamic viscosity of water
The Re and its corresponding water speeds are listed in Table 3.

Table 3. relation between Re and flow speed.

Velocity (m/sec)	Re
1	25002.1
1.5	37503.2
2	50004.2
2.5	62496.8
3	74997.9

The percentage differences between the numerical and experimental results is calculated by the following formula

$$Difference\ \% = \left(\frac{|R_{Exp} - R_{Num}|}{R_{Exp}}\right) * 100 \quad (10)$$

Where $R = \frac{Q_{air}}{Q_{water}}$. The domain outlet is defined as outlet pressure.

Case 01: Triangular Plate

The 1st validation cases are conducted for triangular plate with different dimensions. The geometry is developed as shown in Figure 5**.** Different flow rates are applied for a triangular side length of 10 mm, 13.4 mm, and 16.8 mm. The air-water discharge ratio is recorded for all cases, as listed in
Table **4**.
Comparing the experimentally measured air flow rate and air–to–water flow ratio with the corresponding numerical predictions. For all geometries, the numerical model captures the variation in air entrainment with

Figure 5. Orifice with Triangular plate section.

reasonable accuracy, as reflected by the relatively small percentage differences between experimental and CFD values. The triangular orifice with 10 mm side length exhibits deviations ranging approximately from 0.08% to 2.17%, indicating strong agreement across the tested operating conditions. Similarly, the 13.4 mm configuration shows very close correspondence, with all differences below 2.5% and one case reaching near-perfect agreement. The 16.8 mm orifice generally maintains acceptable accuracy; however, a slightly larger deviation appears at higher flow conditions, which may be attributed to increased flow unsteadiness and complex phase interaction downstream of the larger opening. Overall, the tabulated results demonstrate that the numerical model reliably predicts both the air flow rate and the normalized flow ratio for different geometric configurations.

Table 4. Validation for Triangular orifice side length 10 mm

Side Length [mm]	$Q_{air\_Exp}\ [x10^{-3}]$	R_{Exp}	$Q_{air\_Num}\ [x10^{-3}]$	R_{Num}	Difference %
10	0.476	0.970	0.478	0.974	0.42
	0.633	0.860	0.6325	0.859	0.08
	0.79	0.805	0.776	0.791	1.77
	0.877	0.715	0.858	0.700	2.17
	1.012	0.688	1.03	0.700	1.78

13.4	0.425	0.866	0.428	0.872	0.71
	0.5495	0.747	0.538	0.731	2.09
	0.674	0.687	0.658	0.671	2.37
	0.7675	0.626	0.767	0.625	0.07
	0.9075	0.617	0.897	0.609	1.16
16.8	0.448	0.913	0.4539	0.925	1.32
	0.5085	0.691	0.502	0.682	1.28
	0.569	0.580	0.5638	0.575	0.91
	0.6955	0.567	0.653	0.532	6.11
	0.7565	0.514	0.7297	0.496	3.54

Figure 6 illustrates the relationship between the air–to–water flow ratio (Q_{air}/Q_w) and Reynolds number for the three triangular orifice geometries, combining CFD predictions with experimental data points. A consistent decreasing trend in (Q_{air}/Q_w) is observed as the Reynolds number increases, indicating that higher liquid momentum reduces the relative air entrainment through the orifice. The smallest orifice (10 mm) exhibits the highest air–to–water ratio across the Reynolds number range, followed by the 13.4 mm and 16.8 mm plates, highlighting the strong influence of orifice geometry on phase mixing behavior. The close overlap between numerical curves and experimental markers confirms the capability of the CFD model to reproduce the overall trend and magnitude of the multiphase interaction. Minor discrepancies at higher Reynolds numbers, particularly for the largest orifice, suggest increased turbulence intensity and interface instability, which may introduce additional experimental uncertainties and modeling challenges.

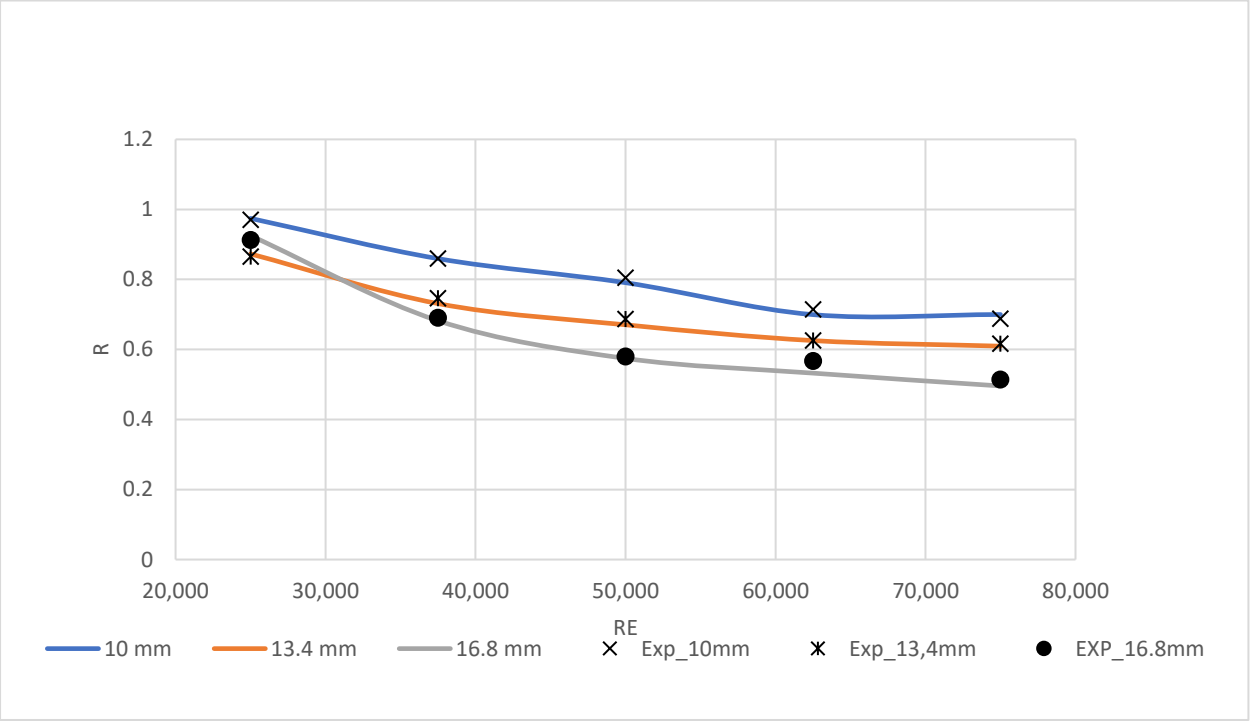

Figure 6. CFD and experiment results for triangular orifice plate.

Case 02: Square Plate Validation

The square plate geometry is shown in Figure 7. The analyses are conducted for the orifice with square plate at three side lengths including 6.7 mm, 8.9 mm, and 11.1 mm, at different mass flow rates.

Figure 7. Square Geometry

Table ***5*** summarizes the validation results for square orifice plates with characteristic lengths of 6.7 mm, 8.9 mm, and 11.1 mm, presenting a comparison between experimental measurements and numerical predictions of the air flow rate and the normalized air–to–water flow ratio. Across all three geometries, the CFD model demonstrates strong predictive capability, with most percentage differences remaining below approximately 1.5% and only a few cases approaching slightly higher deviations. The 6.7 mm square orifice exhibits particularly close agreement, with minimal discrepancies that confirm accurate representation of the interfacial flow behavior. The 8.9 mm configuration shows similarly consistent trends, including an exact match in one operating condition, indicating robustness of the numerical formulation. For the 11.1 mm orifice, the agreement remains satisfactory, although minor deviations appear at higher flow conditions, likely due to enhanced turbulence intensity and increased sensitivity of the larger opening to phase interaction effects.

Table 5. Validation For Square Orifice Length 6.7 mm

Side Length [mm]	$Q_{air\_Exp}\ [x10^{-3}]$	R_{Exp}	$Q_{air\_Num}\ [x10^{-3}]$	R_{Num}	**Difference %**
6.7	0.3355	0.684	0.3306	0.674	1.46
	0.4167	0.566	0.416	0.565	0.17
	0.4978	0.507	0.4969	0.506	0.18
	0.5813	0.474	0.579	0.472	0.40
	0.6797	0.462	0.6747	0.458	0.74
8.9	0.307	0.626	0.312	0.636	1.63
	0.358	0.486	0.37	0.503	3.35
	0.409	0.417	0.408	0.416	0.24
	0.477	0.389	0.475	0.387	0.42
	0.57	0.387	0.577	0.392	1.23
11.1	0.236	0.481	0.238	0.485	0.85
	0.3008	0.409	0.302	0.410	0.40
	0.3657	0.373	0.367	0.374	0.36
	0.432	0.352	0.429	0.350	0.69
	0.5077	0.345	0.5012	0.341	1.28

As shown in Figure 8, the plotted results illustrate the variation of the air–to–water flow ratio with Reynolds number for the three-square geometries, combining CFD curves with experimental results. A clear decreasing trend is observed for all configurations as the Reynolds number increases, reflecting the dominance of liquid momentum over air entrainment at higher flow rates. The smallest square orifice (6.7 mm) consistently produces the highest (Q_{air}/Q_w), followed by the 8.9 mm and 11.1 mm plates, demonstrating the strong influence of orifice size on multiphase mixing performance. The close alignment between numerical and experimental data across the Reynolds number range validates the modeling approach and indicates that the selected multiphase formulation

successfully captures the overall behavior of the gas–liquid interaction. Minor divergence between curves at higher Reynolds numbers suggests increased flow complexity and possible experimental uncertainties associated

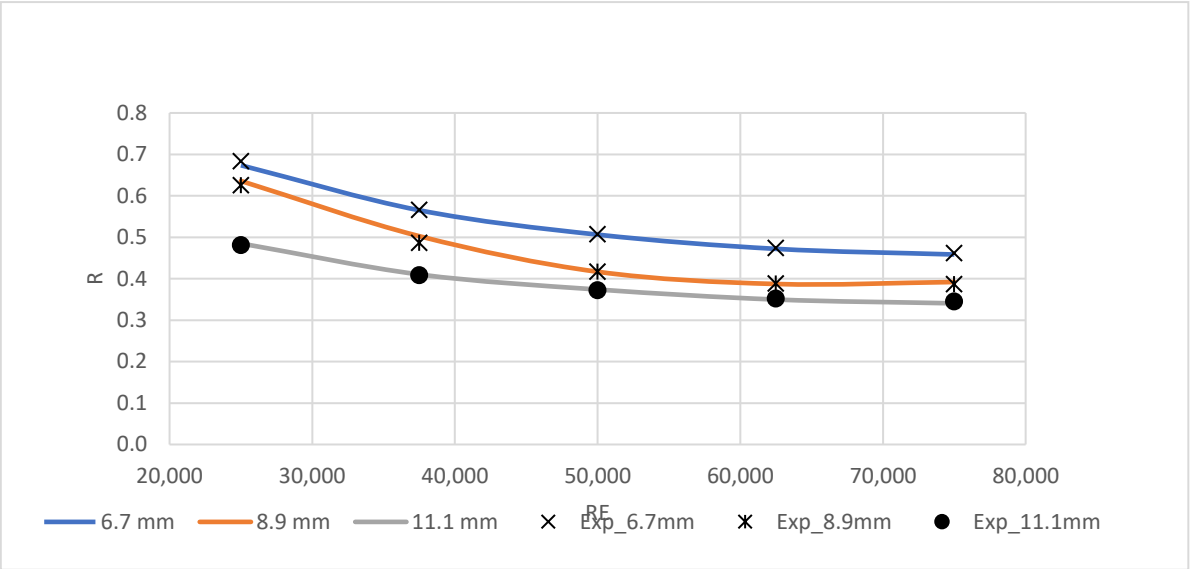

with interface fluctuations and local turbulence effects. The streamlines are depicted in Figure 9.

Figure 8. Square plate CFD-Experiment validation.

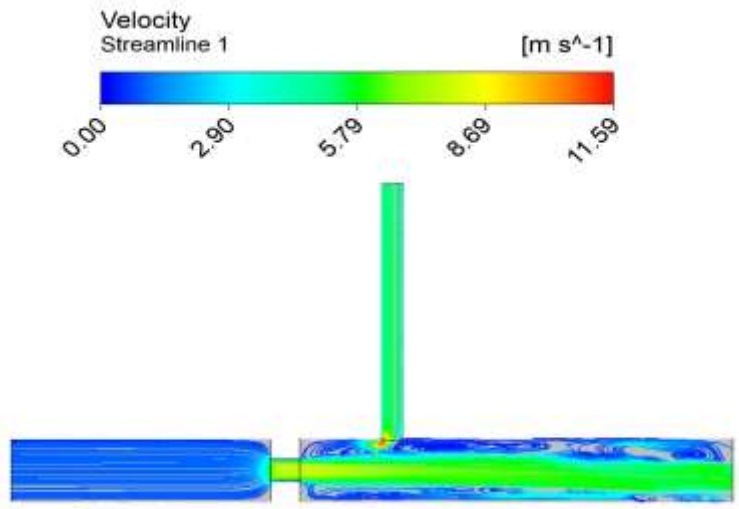

Figure 9. Flow streamlines for square orifice L 8.9 mm 1st case.

The standard uncertainty associated with the measured air flow rate is evaluated following the Equation [33], [34],

$u_Q = \frac{A}{\sqrt{3}}$ (11)

Where A is the manufacturer's specified accuracy of the flow meter expressed as a percentage of the reading. The subscript Q refers to the flow (i.e. water or air). Accordingly, the combined uncertainty propagated from the water and air flowmeters can be expressed as follows:

$u = \sqrt{u_{air}^2 + u_{water}^2} = \sqrt{1.443^2 + 0.577^2} = 1.55\%$ (4)

The standard uncertainties of the air and water flowmeters are estimated from the accuracy limits specified by the manufacturers (listed in

Table **6**). The expanded uncertainty is then calculated as $U_Q = ku_Q$, where a coverage factor of $k = 2$ is adopted (i.e. $U_Q = 2 * 1.55 = 3.1\%$), corresponding approximately to a 97% confidence level.

Table 6. uncertainty analysis

Quantity	**Instrument accuracy (A)**	**Standard uncertainty (u_Q)**
Air flow meter	±2.5%	±1.443%
Water flow meter	±1.0%	±0.577%
Accumulated accuracy	u	±1.55%
Expanded uncertainty, (k=2)	k*u	±3.11%

*k is a convergence factor

4 Results and Discussion

The CFD analyses are conducted for orifice plates with circular, square, and triangular openings at different dimensions and flow rates. For the circular orifice plate, the first case ($D = 7.5$ mm, $Re = 25002.1$) is adopted as the baseline design, with a numerical air-to-water discharge ratio of $(Q_{air}/Q_{water})_{Num} = 0.4286$. The normalized discharge ratio, defined as $R^* = (Q_{air}/Q_{water})_{case}/(Q_{air}/Q_{water})_{baseline}$, therefore equals 1.000 for the baseline case. For $D = 7.5$ mm, R^*decreased from 1.000 to 0.725 as the operating condition increased, indicating a reduction in relative air-entrainment performance. For $D = 10$ mm, the normalized ratio ranged from 0.602 to 0.800, while for $D = 12.5$ mm, it ranged from 0.559 to 0.925. Overall, all circular-orifice cases produced lower air-to-water discharge ratios than the baseline, with the largest reduction observed for the $D = 12.5$ mmcase at $R^* = 0.559$. The air inlet was positioned at the first air-inlet location for all cases.

Table 7. Discharge ratios for circular orifice plates with different diameters.

D [mm]	Q_{air_Num} $[x10^{-3}]$	R_{Num}	R^*
7.5	0.21	0.4286	1.000
	0.29	0.394	0.919
	0.359	0.3658	0.853
	0.397	0.3236	0.755
	0.457	0.3106	0.725
10	0.160	0.3261	0.761
	0.239	0.3247	0.758
	0.337	0.343	0.800
	0.360	0.2935	0.685
	0.380	0.2582	0.602
12.5	0.195	0.3964	0.925
	0.231	0.3138	0.732
	0.247	0.2517	0.587
	0.294	0.2397	0.559
	0.39	0.265	0.618

Figure 10 further illustrates the effect of Reynolds number on the discharge performance of the circular orifices. Overall, R decreases with increasing Re, indicating a reduction in relative air entrainment at higher flow rates. This decline is most pronounced for the 12.5 mm orifice, where the ratio decreases sharply before approaching a more stable value at higher Reynolds numbers. The 10 mm orifice exhibits a mildly nonlinear response, with a slight increase at intermediate Reynolds numbers followed by a subsequent decrease. In contrast, the 7.5 mm orifice maintains the highest and most stable discharge ratio over the investigated range. This behavior suggests that smaller orifices promote stronger air induction by generating higher local velocities, sharper pressure gradients, and more intense shear-driven mixing, whereas larger openings weaken entrainment mechanisms and produce lower normalized discharge ratios. The pressure and velocity contours for the D = 10 mm circular-orifice case are presented in Figure 11.

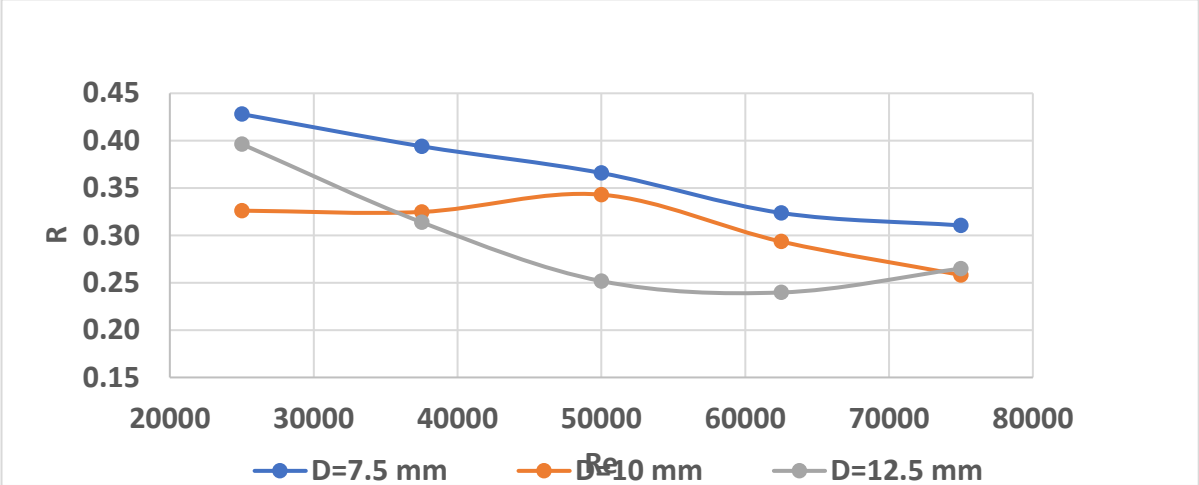

Figure 10. Discharge ratio for circular orifice plate with different diameters.

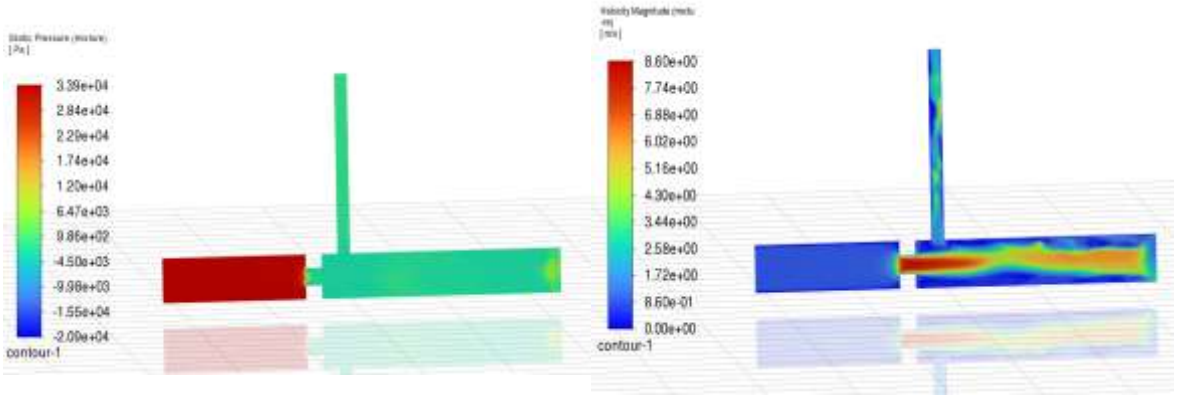

(a) Pressure contours (b) Velocity contours

Figure 11. Circular hole pressure and velocity contours D 10 mm 1st case

Solution Methods and Convergence Criteria

For all cases, the transient CFD simulations are performed using a pressure-based solver with the VOF multiphase model to capture the air–water interface. Turbulence is modeled using the realizable k–ε model with scalable wall functions to represent shear-layer development and recirculation downstream of the orifice. Pressure–velocity coupling is handled using the coupled algorithm, and the pressure equation is discretized with the PRESTO! scheme because of its suitability for multiphase flows with strong pressure gradients. Gradients are evaluated using the least-squares cell-based method. The momentum, turbulent kinetic energy, and turbulent dissipation rate equations are discretized using the first-order upwind scheme, whereas the volume-fraction equation is solved using the compressive interface-capturing scheme to preserve a sharp air–water interface. The transient term is treated using a first-order implicit formulation to improve numerical stability.

Solution convergence is assessed using both residual reduction and the temporal stability of the monitored air discharge, Q_a. At each time step, the governing equations are iterated until the specified residual criteria are satisfied or the maximum number of inner iterations is reached. In addition, Q_a is monitored as the primary integral convergence indicator because it directly reflects the air-entrainment performance of the orifice system. As shown in Figure 12 for the circular orifice with $D = 10$mm, the air-discharge history initially exhibits pronounced oscillations, including short-term reverse-flow fluctuations, which correspond to the development of the air–water interface, jet contraction, and suction region downstream of the orifice. After approximately 60 s, Q_a approaches a quasi-stable fluctuating regime with comparatively small variations, indicating that the entrainment process has reached statistically steady behavior. Therefore, the reported air-discharge values are extracted from the stabilized portion of the Q_a-time curve after the initial transient period, thereby minimizing start-up effects and ensuring consistent comparison among the investigated orifice configurations.

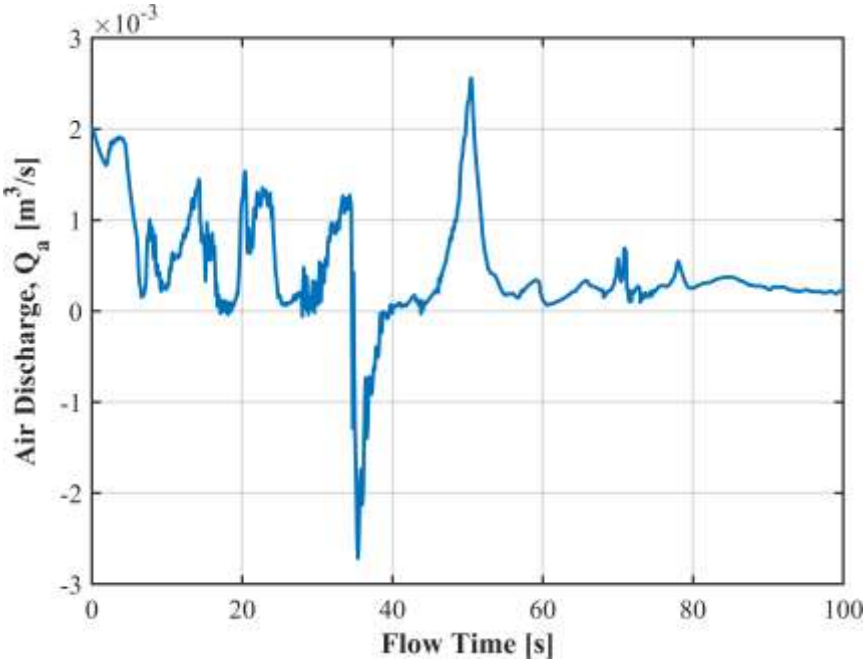

Figure 12. Air discharge vs flow time for Circular Orifice D 10 mm case 01.

The numerical results for the square orifice plate, listed in

Table ***8***, show that the air-to-water discharge ratio is strongly affected by the side length L. Relative to the baseline circular orifice case, the smallest square opening ($L = 6.7$ mm) provides the highest normalized discharge performance, with R^* ranging from 1.029 to 1.322. This indicates that the smaller square opening enhances air entrainment compared with the baseline circular case, primarily because of stronger jet contraction, higher local velocity, and sharper pressure reduction along the orifice edges. For the intermediate opening ($L = 8.9$ mm), R^* ranges from 0.840 to 1.189, indicating moderate entrainment performance with a non-monotonic response. This behavior suggests a balance between the larger flow area, which reduces local acceleration, and the sharp-edged geometry, which maintains shear-driven air induction. In contrast, the largest square opening ($L = 11.1$ mm) produces lower normalized ratios, ranging from 0.814 to 0.956, showing that increasing the side length weakens the relative suction effect despite allowing higher absolute air discharge.

Figure 13 further illustrates the influence of Reynolds number on the discharge behavior of the square orifices. For $L = 6.7$ mm, the discharge ratio decreases gradually with increasing Reynolds number, indicating a reduction in normalized entrainment efficiency at higher flow rates. The $L = 8.9$ mmcase exhibits a nonlinear trend, with improved performance at intermediate Reynolds numbers before decreasing to higher values. The $L = 11.1$ mmorifice maintains a comparatively low and stable response, reflecting weaker pressure gradients and reduced interfacial mixing intensity. Overall, the results demonstrate that smaller square orifices can outperform the baseline circular design in terms of normalized air entrainment because their sharp corners and reduced opening area promote stronger contraction, suction, and turbulence generation.

Table 8. Discharge ratio for square orifice holes with different side lengths.

L [mm]	**Q_{air_Num} [x10^{-3}]**	**R_{Num}**	**R^***
6.7	0.278	0.5665	1.322
	0.395	0.5367	1.252
	0.453	0.462	1.078
	0.554	0.452	1.055
	0.649	0.441	1.029
8.9	0.237	0.483	1.127
	0.348	0.473	1.104
	0.5	0.5095	1.189
	0.493	0.40196	0.938
	0.53	0.3601	0.840
11.1	0.179	0.365	0.852

	0.302	0.41	0.956
	0.35	0.356	0.830
	0.46	0.375	0.875
	0.514	0.349	0.814

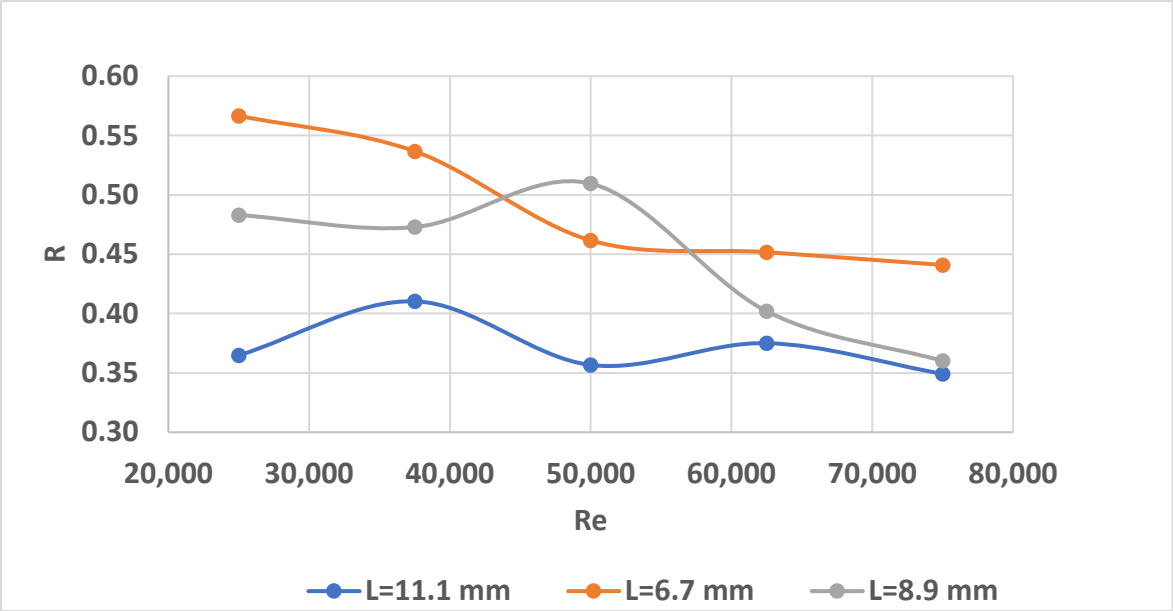

Figure 13. Discharge ratio for square orifice holes with different side lengths.

Figure 14 presents the variation of the air-to-water discharge ratio with Reynolds number for triangular orifices with characteristic side lengths of 10, 13.4, and 16.8 mm. Relative to the baseline circular orifice, all triangular configurations exhibit higher normalized discharge ratios, indicating superior air-entrainment performance. The smallest triangular orifice ($L = 10$ mm) provides the highest response, with R^* ranging from 1.713 to 2.188. This enhanced performance is attributed to the sharp triangular corners, which intensify jet contraction, shear-layer development, vortex formation, and local pressure reduction downstream of the orifice. These effects strengthen the suction mechanism and promote more effective air induction through the vertical inlet.

For the intermediate triangular orifice ($L = 13.4$ mm), R^* ranges from 1.431 to 1.806, indicating reduced but still substantial improvement relative to the circular baseline. The largest triangular orifice ($L = 16.8$ mm) shows the lowest normalized performance among the triangular cases, with R^* ranging from 1.239 to 1.664. Overall, the discharge ratio decreases as Reynolds number increases, showing that the induced air flow does not increase proportionally with the water discharge. At higher Reynolds numbers, inertial effects, turbulence dissipation, and reduced relative pressure deficit weaken the suction efficiency. Nevertheless, the triangular geometry remains more effective than the baseline circular design because its sharp-edged profile generates stronger contraction, larger pressure gradients, and more intense air–water mixing. The corresponding numerical results are listed in Table 9.

Table 9. Discharge ratios for triangular orifice with different side lengths.

L [mm]	**Q_{air_Num} [x10^{-3}]**	**R_{Num}**	**R^***
10	0.4602	0.938	2.189
	0.648	0.88	2.053
	0.74	0.7541	1.759
	0.9	0.734	1.713
	1.09	0.7406	1.728
13.4	0.38	0.774	1.806
	0.5509	0.7485	1.747
	0.61	0.622	1.451
	0.798	0.651	1.519
	0.903	0.6135	1.431
16.8	0.35	0.713	1.664

	0.477	0.648	1.512
	0.56	0.571	1.332
	0.66	0.538	1.255
	0.782	0.531	1.239

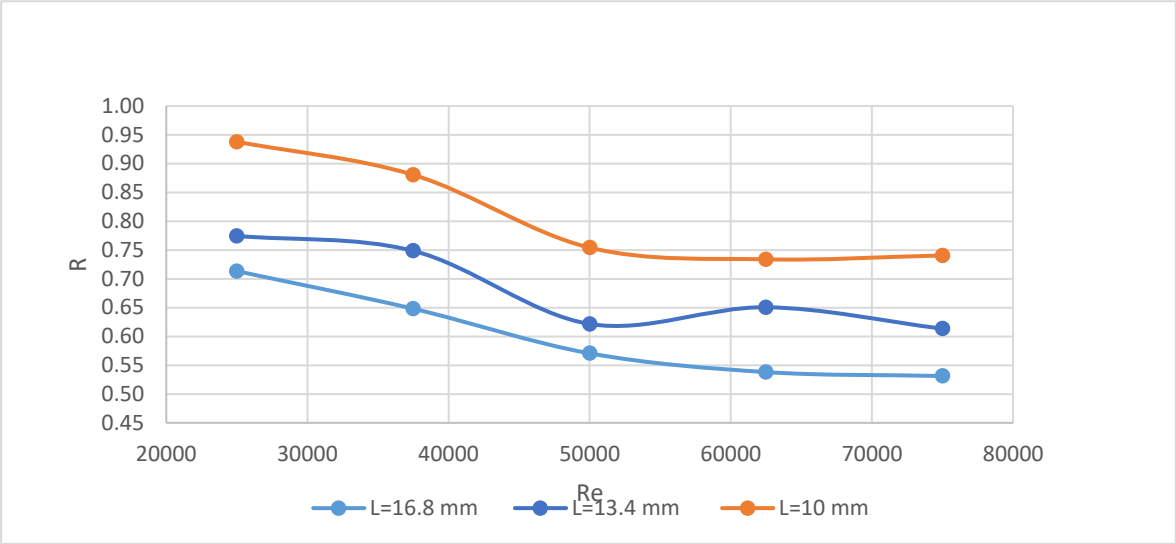

Figure 14. Discharge ratios for triangular orifice with different side lengths.

The streamline and pressure contours in Figure 15 reveal distinct flow features for the circular, square, and triangular orifices. The circular orifice produces a comparatively smoother contraction with a more uniform jet core downstream of the plate. Although a vena contracta forms immediately after the opening, the pressure gradient near the orifice is relatively moderate, resulting in weaker suction at the air-inlet junction and lower air-entrainment capacity. This behavior is consistent with the absence of sharp corners, which limits flow separation, shear-layer instability, and vortex generation.

The square orifice produces stronger contraction and more pronounced flow separation than the circular geometry. Its sharp corners intensify local shear layers and generate additional vortical structures downstream of the plate. Consequently, the pressure contours show a larger low-pressure region near the vena contracta, which enhances air induction compared with the circular orifice. However, the square opening still maintains a relatively wider jet than the triangular case, reducing the magnitude of local acceleration and limiting the suction strength.

The triangular orifice exhibits the most intense contraction and the narrowest downstream jet among the investigated geometries. The streamline contours show strong jet acceleration through the constricted region, while the pressure contours indicate the steepest pressure gradient and the most pronounced low-pressure zone near the vena contracta and air-inlet connection. This response is attributed to the acute vertices of the triangular opening, which promote localized flow separation, stronger shear-layer development, and enhanced vortex formation. These mechanisms increase turbulence production and strengthen the interaction between the high-velocity water jet and the induced air stream.

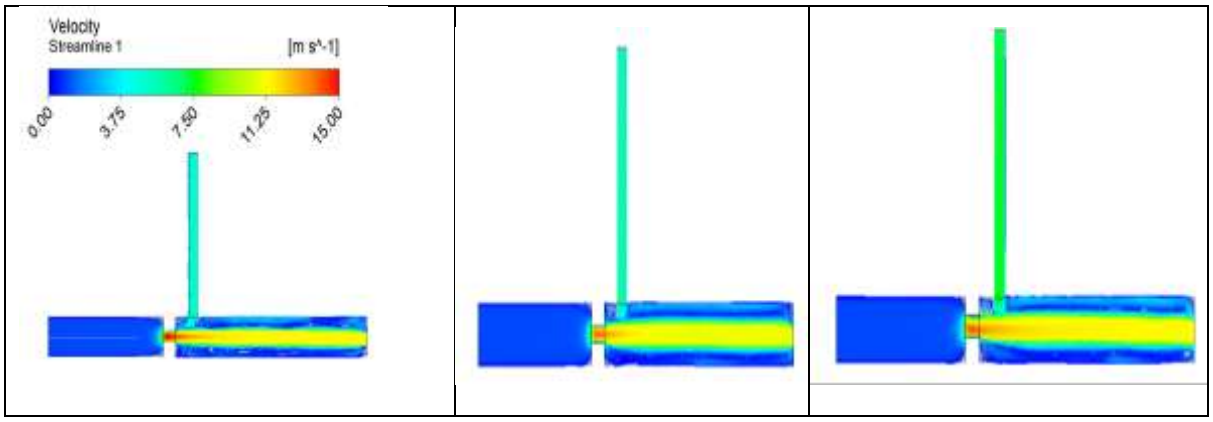

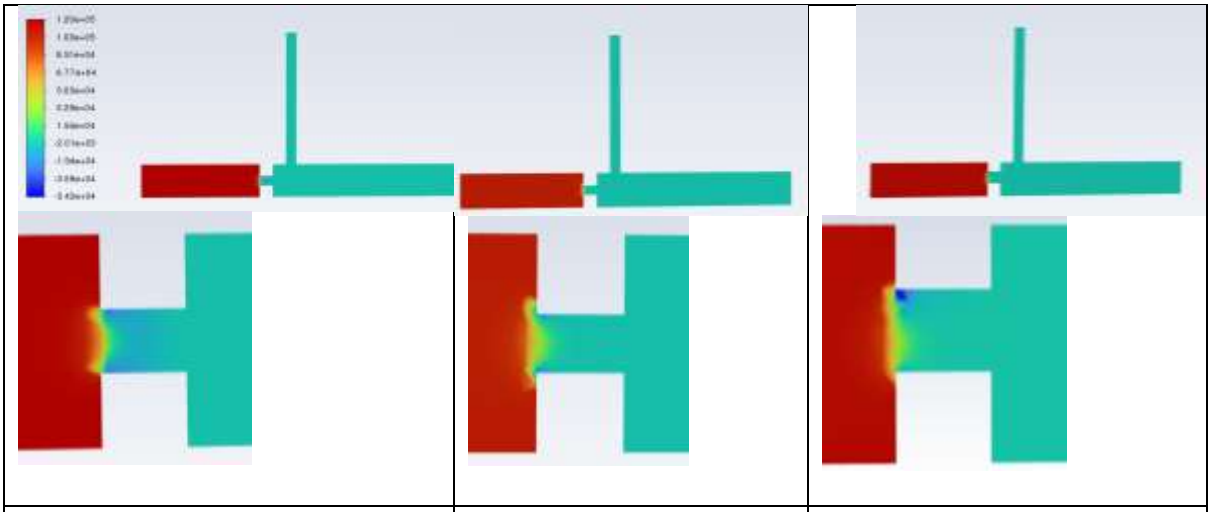

(a) Circular (b) Square (C) Triangular

Figure 15. Circular (a) Square (b) and Triangular (C) orifices streamlines (upper) and pressure (Lower) contours, 1st pipe position.

To investigate the effect of air-inlet position, the air pipe is shifted forward by a distance equivalent to 1.33 times the baseline orifice diameter, while all other geometric parameters are kept unchanged, as shown in Figure 16. This additional parametric analysis is performed only for circular orifice plates. The corrected numerical results, listed in

Table ***10***, show that relocating the air entrance substantially affects the air-to-water discharge ratio, particularly for the smallest orifice. For D = 7.5 mm, the normalized ratio R^* ranges from 0.704 to 1.099. The first operating condition exceeds the baseline circular design by approximately 9.9%, indicating that the shifted inlet can enhance air induction when it is located closer to the low-pressure suction region generated near the vena contracta. However, at higher operating conditions, R^* decreases below unity, suggesting that the forward position becomes less effective as the jet structure and suction zone shift downstream. For D = 10mm, R^*ranges from 0.573 to 0.875, while for D = 12.5mm it ranges from 0.520 to 0.699. These lower values indicate that larger circular openings generate weaker local acceleration and smaller pressure gradients near the air-inlet junction, thereby reducing the effectiveness of suction-driven air entrainment. The results demonstrate that the influence of air-inlet relocation is diameter-dependent, with the strongest sensitivity observed for the smallest circular orifice.

Figure 16. Change the air inlet pipe position.

Table 10. Discharge ratios for circular orifice hole for a moved forward air entrance hole.

D [mm]	Q_{air_Num} [$x10^{-3}$]	R	R^*
7.5	0.2312	0.4712	1.099
	0.271	0.3682	0.859
	0.3	0.3057	0.713
	0.37	0.3017	0.704
	0.47	0.3193	0.745
10	0.184	0.3750	0.875
	0.217	0.2948	0.688
	0.241	0.2456	0.573
	0.32	0.2609	0.609
	0.39	0.2650	0.618

12.5	0.147	0.2996	0.699
	0.184	0.2500	0.583
	0.22	0.2242	0.523
	0.2778	0.2265	0.528
	0.328	0.2229	0.520

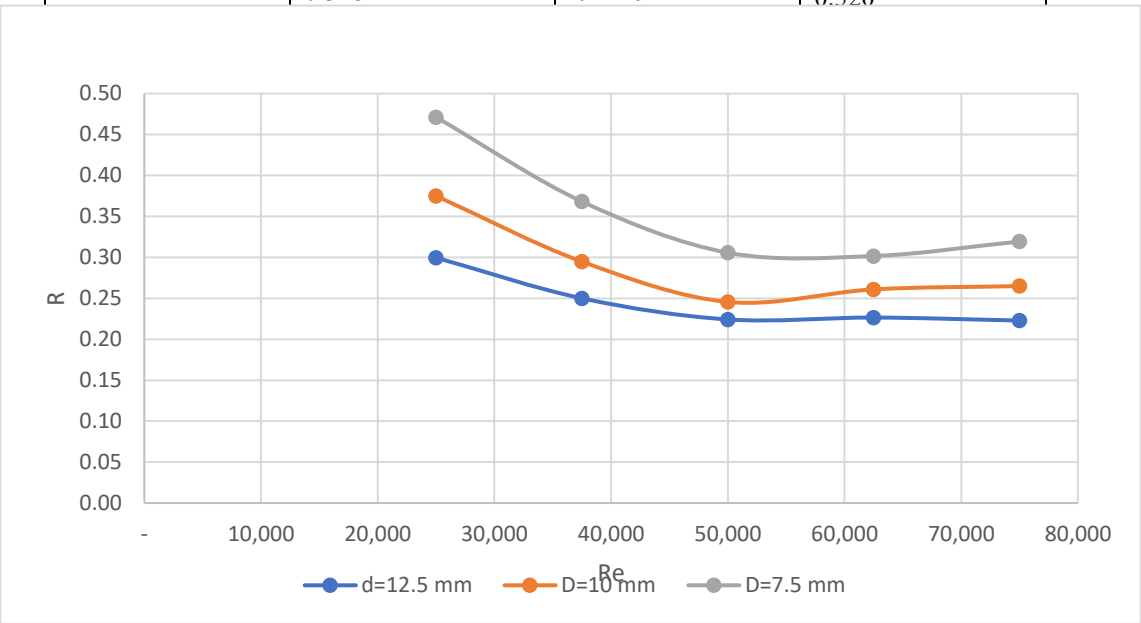

Figure 17. Discharge ratios for circular orifice hole for a moved forward air entrance hole at different diameters.

5 Conclusion

A numerical study is conducted to assess air–water discharge through circular, square, and triangular orifice plates under different dimensions, Reynolds numbers, and air-inlet positions. The CFD model, developed in ANSYS Fluent using the VOF approach and realizable k–ε turbulence model, is validated against experimental data and showed good agreement.

The results indicate that smaller orifices improve the normalized discharge ratio R by increasing jet acceleration, pressure reduction, and air entrainment near the vena contracta. Triangular orifices provided the highest performance, with $R^* = 1.239–2.189$, corresponding to a 23.9–118.9% improvement over the baseline circular case. Square orifices showed moderate enhancement, with $R^* = 0.814–1.322$ and a maximum improvement of 32.2%. The superior performance of triangular openings is attributed to their sharp vertices, which intensify flow contraction, vortex formation, and suction-driven air induction. Increasing Reynolds number generally reduced R, indicating that air entrainment did not increase proportionally with water discharge. Forward shifting the air inlet in circular orifices produced $R^* = 0.520–1.099$, showing that inlet relocation can improve performance by up to 9.9% only when aligned with the low-pressure region. The results reveal that orifice shape, size, Reynolds number, and air-inlet position are critical parameters for optimizing orifice-based aeration and mixing systems.

References

[1] A. S. Almawla, A. H. Kamel, and A. M. Lateef, "Modelling of Flow Patterns over Spillway with CFD (Case Study: Haditha Dam in Iraq)," IJDNE, vol. 16, no. 4, pp. 373–385, Aug. 2021, doi: 10.18280/ijdne.160404.

[2] V. H. P. D. Morais, T. Z. Gireli, and P. Vatavuk, "Numerical and experimental models applied to an ogee crest spillway and roller bucket stilling basin," RBRH, vol. 25, p. e18, 2020, doi: 10.1590/2318-0331.252020190005.

[3] B. Al-Hadeethi, A. S. Almawla, A. H. Kamel, H. A. Afan, and A. N. Ahmed, "Numerical Modeling of Flow Pattern with Different Spillway Locations," MMEP, vol. 11, no. 5, pp. 1219–1226, May 2024, doi: 10.18280/mmep.110510.

[4] V. Jothiprakash, V. V. Bhosekar, and P. B. Deolalikar, "Flow characteristics of orifice spillway aerator: numerical model studies," ISH Journal of Hydraulic Engineering, vol. 21, no. 2, pp. 216–230, May 2015, doi: 10.1080/09715010.2015.1007093.

[5] J. X. Zhang, "Analysis on the effect of venturi tube structural parameters on fluid flow," AIP Advances, vol. 7, no. 6, p. 065315, Jun. 2017, doi: 10.1063/1.4991441.

[6] A. R. Kaladgi, A. Mukhtar, A. Afzal, M. Kareemullah, and M. K. Ramis, "Numerical Investigation of Beta Ratio and Reynolds Number Effect on Coefficient of Discharge of Venturimeter," IOP Conf. Ser.: Mater. Sci. Eng., vol. 884, no. 1, p. 012116, Jul. 2020, doi: 10.1088/1757-899X/884/1/012116.

[7] M. K. Sarwar, I. Ahmad, Z. A. Chaudary, and H.-U.-R. Mughal, "Experimental and numerical studies on orifice spillway aerator of Bunji Dam," Journal of the Chinese Institute of Engineers, vol. 43, no. 1, pp. 27–36, Jan. 2020, doi: 10.1080/02533839.2019.1676652.

[8] T. Höhne and T. Mamedov, "CFD Simulation of Aeration and Mixing Processes in a Full-Scale Oxidation Ditch," Energies, vol. 13, no. 7, p. 1633, Apr. 2020, doi: 10.3390/en13071633.

[9] M. Cao et al., “Effects of discharge angle of jet from a slot orifice on cooling performance for a perforated air ducting system in dairy cattle barn,” Computers and Electronics in Agriculture, vol. 210, p. 107890, Jul. 2023, doi: 10.1016/j.compag.2023.107890.
[10] M. M. Tukiman et al., “CFD simulation of flow through an orifice plate,” IOP Conf. Ser.: Mater. Sci. Eng., vol. 243, p. 012036, Sep. 2017, doi: 10.1088/1757-899X/243/1/012036.
[11] M. Fadaei, A. M. Alahmad, H. Ranjbar, A. Morovati, M. Hosnani, and A. H. Amiri, “EXPERIMENTAL INVESTIGATION AND CFD SIMULATION OF THE ORIFICE FLOW METER TO MEASURE TWO-PHASE FLOW,” BJPG, vol. 18, no. 3, pp. 139–149, Oct. 2024, doi: 10.5419/bjpg2024-0009.
[12] V. Hernandez-Perez, M. Abdulkadir, and B. J. Azzopardi, “Grid Generation Issues in the CFD Modelling of Two-Phase Flow in a Pipe,” The Journal of Computational Multiphase Flows, vol. 3, no. 1, pp. 13–26, Mar. 2011, doi: 10.1260/1757-482X.3.1.13.
[13] A. Golijanek-Jędrzejczyk, A. Mrowiec, R. Hanus, M. Zych, M. Heronimczak, and D. Świsulski, “The assessment of metrological properties of segmental orifice based on simulations and experiments,” Measurement, vol. 181, p. 109601, Aug. 2021, doi: 10.1016/j.measurement.2021.109601.
[14] A. K. D. A. Medeiros, J. F. D. Lima, G. G. D. Medeiros, N. F. D. Silva Junior, R. N. B. Felipe, and R. C. T. D. S. Felipe, “Parameters for dimensional inspection of orifice plates and roughness of the straight stretches of the tubing,” Braz. arch. biol. technol., vol. 49, no. spe, pp. 1–8, Jan. 2006, doi: 10.1590/S1516-89132006000200002.
[15] W. Jitschin, “Gas flow measurement by the thin orifice and the classical Venturi tube,” Vacuum, vol. 76, no. 1, pp. 89–100, Oct. 2004, doi: 10.1016/j.vacuum.2004.05.014.
[16] M. A. R. Eltoukhy and M. O. Alsaydalani, “INVESTIGATION OF THE DISCHARGE COEFFICIENT FOR ORIFICE AND PIPE BEHAVIOR,” vol. 17, 2022.
[17] Dhairyashil Dhumal, Yashwant More, Ujwal Gawai, and Imperial Collage Of Engineering Research, “Design, Fabrication CFD Analysis of Multi-Hole Orifice Plate,” IJERT, vol. V6, no. 06, p. IJERTV6IS060161, Jun. 2017, doi: 10.17577/IJERTV6IS060161.
[18] J. Almutairi, A. Hasečić, and E. Džaferović, “Numerical Analysis of Newtonian Fluid Flow Through Multi-Hole Orifice Meter,” presented at the The 9th World Congress on Mechanical, Chemical, and Material Engineering, Aug. 2023. doi: 10.11159/htff23.182.
[19] V. K. Singh and T. John Tharakan, “Numerical simulations for multi-hole orifice flow meter,” Flow Measurement and Instrumentation, vol. 45, pp. 375–383, Oct. 2015, doi: 10.1016/j.flowmeasinst.2015.08.004.
[20] H. Düz, “Numerical optimization of bevel angle in conical entrance multihole plates to reduce pressure losses,” Flow Measurement and Instrumentation, vol. 102, p. 102778, Mar. 2025, doi: 10.1016/j.flowmeasinst.2024.102778.
[21] A. Baylar, “An Investigation on the Use of Venturi Weirs as an Aerator,” Water Quality Research Journal, vol. 38, no. 4, pp. 753–767, Nov. 2003, doi: 10.2166/wqrj.2003.047.
[22] Research Scholar, Department of Agricultural Engineering, Triguna Sen School of Technology, Assam University Silchar, Assam -788011, India, A. Yadav, A. Kumar, Assistant Professor, Department of Agricultural Engineering, Triguna Sen School of Technology, Assam University Silchar, Assam -788011, India, S. Sarkar, and Associate Professor, Department of Agricultural Engineering, Triguna Sen School of Technology, Assam University Silchar, Assam -788011, India, “Design Characteristics of Venturi Aeration System,” IJITEE, vol. 8, no. 11, pp. 63–70, Sep. 2019, doi: 10.35940/ijitee.J9929.0981119.
[23] A. Yadav, A. Kumar, and S. Sarkar, “Performance evaluation of venturi aeration system,” Aquacultural Engineering, vol. 93, p. 102156, May 2021, doi: 10.1016/j.aquaeng.2021.102156.
[24] M. Cihat Tuna, F. Ozkan, and A. Baylar, “Experimental investigations of aeration efficiency in high-head gated circular conduits,” Water Science and Technology, vol. 69, no. 6, pp. 1275–1281, Mar. 2014, doi: 10.2166/wst.2014.021.
[25] Y. Guo, L. Zhang, L. Yu, S. Luo, C. Liu, and Y. Liu, “The Impact of Decreased Atmospheric Pressure on Forced Aeration of Discharged Flow,” Water, vol. 16, no. 2, p. 353, Jan. 2024, doi: 10.3390/w16020353.
[26] S. Felder and H. Chanson, “Aeration and air–water mass transfer on stepped chutes with embankment dam slopes,” Environ Fluid Mech, vol. 15, no. 4, pp. 695–710, Aug. 2015, doi: 10.1007/s10652-014-9376-x.
[27] H. Wan, R. Li, C. Gualtieri, H. Yang, and J. Feng, “Numerical Simulation of Hydrodynamics and Reaeration over a Stepped Spillway by the SPH Method,” Water, vol. 9, no. 8, p. 565, Jul. 2017, doi: 10.3390/w9080565.
[28] T. Bagatur, A. Baylar, and N. Sekerdag, “The Effect of Nozzle Type on Air Entrainment by Plunging Water Jets,” Water Quality Research Journal, vol. 37, no. 3, pp. 599–612, Aug. 2002, doi: 10.2166/wqrj.2002.040.
[30] D. Puri et al., “Performance analysis and modelling of circular jets aeration in an open channel using soft computing techniques,” Sci Rep, vol. 14, no. 1, p. 3140, Feb. 2024, doi: 10.1038/s41598-024-53407-3.
[31] T. Ahmad, S. L. Plee, and J. P. Myers, “FLUENT Theory Guide,” ANSYS, p. 826, 2011.
[32] C. W. Hirt and B. D. Nichols, “Volume of fluid (VOF) method for the dynamics of free boundaries,” Journal of Computational Physics, vol. 39, no. 1, pp. 201–225, Jan. 1981, doi: 10.1016/0021-9991(81)90145-5.
[33] A. Golijanek-Jędrzejczyk, A. Mrowiec, R. Hanus, M. Zych, and D. Świsulski, “Uncertainty of mass flow measurement using centric and eccentric orifice for Reynolds number in the range 10,000 ≤ Re ≤ 20,000,” Measurement, vol. 160, p. 107851, Aug. 2020, doi: 10.1016/j.measurement.2020.107851.
[34] A. Golijanek-Jędrzejczyk, D. Świsulski, R. Hanus, M. Zych, and L. Petryka, “Uncertainty of the liquid mass flow measurement using the orifice plate,” Flow Measurement and Instrumentation, vol. 62, pp. 84–92, Aug. 2018, doi: 10.1016/j.flowmeasinst.2018.05.012.